International Journal of Heat and Mass Transfer 52 (2009) 4221–4228

Contents lists available at ScienceDirect

International Journal of Heat and Mass Transfer

journal homepage: www.elsevier.com/locate/ijhmt

Temperature imaging of sub-millimeter-thick water using a near-infrared camera

Naoto Kakuta [a,*], Katsuya Kondo [b], Atsushi Ozaki [c], Hidenobu Arimoto [d], Yukio Yamada [e]

[a] Department of Applied Quantum Physics and Nuclear Engineering, Faculty of Engineering, Kyushu University, 6-10-1 Hakozaki, Higashi-ku, Fukuoka 812-8581, Japan
[b] Department of Information and Electronics, Graduate School of Engineering, Tottori University, 4-101 Koyama-Minami, Tottori 680-8552, Japan
[c] Graduate School of Systems Life Sciences, Kyushu University, 6-10-1 Hakozaki, Higashi-ku, Fukuoka 812-8581, Japan
[d] Photonic Research Institute, National Institute of Advanced Industrial Science and Technology, 1-2-1 Namiki, Tsukuba 305-8564, Japan
[e] Department of Mechanical Engineering and Intelligent Systems, University of Electro-Communications, 1-5-1 Chofugaoka, Chofu, Tokyo 182-8585, Japan

ARTICLE INFO

Article history:
Received 10 September 2008
Received in revised form 20 February 2009
Accepted 10 April 2009
Available online 3 June 2009

Keywords:
Temperature imaging
Near-infrared camera
Water
Absorbance

ABSTRACT

This paper presents a method of imaging temperature distributions of sub-millimeter-thick water using a near-infrared camera and optical narrow-bandpass filter. The principle is based on the temperature dependence of the $\nu_1 + \nu_3$ absorption band of water. Temperature images are constructed by measuring the absorbance of water at the wavelength of 1412 nm through the filter for all pixels of the camera. From calibration measurements on 0.5-mm thick water at temperatures from 26.0 °C to 40.0 °C, the temperature coefficient was $6.3 \times 10^{-4}\,K^{-1}$ and the standard deviation of absorbance was 1.9×10^{-4}. Thermal diffusion in 0.5-mm thick water caused by a thin heating wire was visualized with this method. The obtained images were verified against temperature distributions calculated by solving a two-dimensional thermal conduction model. This method would be useful for temperature measurement applications and control of aqueous solutions in microchips.

1. Introduction

Temperature monitoring of small amounts of liquid in micro-chemical chips or micro-fluidic chips is being requested in the prospect of expanding applications of micro-total analysis systems (μ-TAS) [1]. Temperature monitoring can be a way of detecting chemical and biochemical reactions inducing heat [2–7] and for controlling thermal conditions in chemical analyses such as the micro-polymerase chain reaction (PCR) [8–10]. A lot of attempts have been made at using micropatterned sensors, e.g., thermopiles, on a microchip to make temperature measurements [2,5–7]. However, because of their complicated fabrication process, possible contamination of the working fluid, and high cost of manufacture, such contact-type sensors have limited uses. In addition, because the measurements are made only at the particular positions of the sensors, these sensors cannot be used to obtain an image of the temperature distribution.

Conventional infrared (IR) imaging might be a good choice for non-contact measurement and imaging of temperature. Fudym et al. [11] obtained IR images of microchip with 25-μm deep microchannels filled with water that were locally heated by a neighboring resistive film and managed to quantify temperature differences in the water by using the Laplacian of the field. However, detecting changes in the temperature of a liquid in a microchip is considerably more difficult than on a solid surface because IR radiation from the liquid is overwhelmed by radiation from the microchip's materials such as glass, poly-dimethyl siloxane (PDMS), and poly-methylmethacrylate (PMMA). Most of these materials are transparent to visible light but absorb mid- and far-IR radiation [12,13], which means they emit radiation with the same wavelength. Hsieh et al. [10] obtained IR images of mineral oil in a microfabricated PCR chamber without a cover, i.e., an open chamber, and used them to evaluate the temperature uniformity in the chamber.

Besides the IR method, several other non-contact methods have been proposed [14]. Micro-Raman thermometry, for example, has a fast response and good stability. Kim et al. [9] used this method to measure temperatures at several points in water inside a microchannel of a PCR chip. However, micro-Raman thermometry needs sophisticated and expensive apparatus. Furthermore, it has not been developed for imaging.

Temperature-dependent particles or dyes might fulfill the requirements for such imaging. Indeed, Kim et al. [15] presented a laser-induced fluorescence thermometry technique for micro-scale temperature imaging. Chapman et al. [16] used two biological membrane probes, 7-nitrobenz-2-oxa-1,3-diazol-4-yl (NBD) and 6-dodecanoyl-2-dimethylamino-naphthalene (laurdan), as thermometers in single living cells. Slyadnev et al. [17] used a fluorescence-quenching technique with rhodamine 3B dye for temperature imaging of the working liquid inside a microchannel. Kachynski et al. [18] demonstrated the possibility of temperature measurements using rhodamine 640 and its anti-stokes luminescence and tried to measure the temperatures of biological cells. Moreover, high-thermo-

* Corresponding author. Tel./fax: +81 92 642 3983.
E-mail address: kakuta@nucl.kyushu-u.ac.jp (N. Kakuta).

0017-9310/$ - see front matter © 2009 Elsevier Ltd. All rights reserved.
doi:10.1016/j.ijheatmasstransfer.2009.04.024

Nomenclature

A	absorbance	M	heat production rate, W/m^2
a_A	temperature coefficient for A, K^{-1}	T	temperature, K
a_B	temperature coefficient for B, K^{-1}	T_a	air temperature, K
B	absorbance for J	t	time, s
c	specific heat capacity, J/(kg K)		
h_a	convective heat transfer coefficient, W/(m^2 K)	*Greek symbols*	
I	spectral intensity of transmitted light	α	spectral absorbance of sample holder
I_r	spectral intensity of transmitted light for reference	ε	noise intensity
I_0	spectral intensity of incident light	λ	wavelength of light, m
J	intensity of pixel signal	λ_T	wavelength of light for temperature-dependence, m
J_r	intensity of pixel signal for reference	ρ	mass density, kg/m^3
k	thermal conductivity, W/(m K)	τ	spectral transmittance of filter

sensitivity fluorescent polymers are being developed [19]. Despite these advances, the use of fluorescent materials is accompanied by quenching and discoloration problems. In addition, extrinsic substances are not always able to be mixed into a liquid sample because of their impurity or toxicity. To avoid mixing, Muwanga and Hassan [20] used an un-encapsulated thermochromic liquid crystal layer mounted in the vicinity of the microchannel walls. They described, however, that it was very difficult to handle the liquid crystal and to obtain reliable calibration data.

The authors have been studying a convenient non-contact way of using near-infrared spectroscopy (NIRS) for measuring the temperature of aqueous solutions [21–23]. This method is based on the temperature dependence of the near-infrared (NIR) absorption of water. For example, the peak of the absorption band of water near the wavelength of 1440 nm ($\nu_1 + \nu_3$ band), corresponding to the combination of symmetric and antisymmetric O–H stretching vibrational modes of water molecules, shifts to a shorter wavelength when the temperature increases [24–27]. The temperature dependence has been known in NIR spectrometry in biomedical, agricultural, and polymer sciences, but it has usually been regarded as a disturbance. While some experimenters have made use of it to measure the temperature of various samples that contain water [23,25,28–30], others have tried to cancel out the temperature effect in noninvasive measurements of glucose concentration *in vivo* [31–34].

An important advantage of an NIRS-based method is that it can obtain a temperature averaged over the light path within the medium, i.e., an average including internal temperatures. This is different from conventional IR thermometry, which essentially detects only surface temperatures. Another advantage is that the power of the irradiation light can be adjusted according to sample conditions such as thickness, area, and absorbance. Fortunately, most microchip materials are nearly transparent to NIR light [35–37], and the possibility of measuring the temperature of aqueous solutions in microchannels has been indicated [3]. Also, neither excitation light nor marker particle is needed. Despite these apparent advantages, to our knowledge, no one has yet tried to develop an NIRS method of temperature imaging.

This paper presents an NIRS method of imaging temperature distributions using an indium gallium arsenide (InGaAs) camera sensitive to the wavelength range from 900 nm to 1700 nm and an optical narrow-bandpass filter. At present, CCD (charge coupled device) and CMOS (complementary metal oxide semiconductor) cameras cannot cover this wavelength range. First, we acquired temperature images of temperature-controlled 0.5-mm thick water in order to calibrate the signals against temperature. Next, we locally heated the water by immersing a thin hot wire in it [18,21] and obtained temperature images. The most effective way of verifying the obtained images is numerical simulation. Therefore, we compared the measured results with calculated ones.

2. Methods

2.1. Principle

The NIR region has several absorption bands derived from overtones and combinations of fundamental resonances of water molecule vibrations. One of them is an absorption band near the wavelength of 1440 nm, which corresponds to the combination of symmetric and antisymmetric O–H stretching modes, ν_1 (ca. 3657 cm^{-1}) + ν_3 (ca. 3756 cm^{-1}) [24]. Fig. 1 shows the absorbance spectra of 0.5-mm thick water at different temperatures, where the $\nu_1 + \nu_3$ band is seen. The absorbance, A is defined as

$$A(\lambda, T) = -\log_{10}\frac{I(\lambda, T)}{I_0(\lambda)} - \alpha(\lambda), \tag{1}$$

where λ is the wavelength of light, T is the temperature of water, and I and I_0 are, respectively, the intensities of light transmitted through the water and its holder and of incident light. The last term, α is the absorbance of the sample holder, e.g., a quartz cuvette, including reflection losses from the surfaces. Note that α does not appear in a normal definitional equation for absorbance, but we have assumed that the incident light is observed outside a sample holder.

Fig. 1 also reveals that the peak of the absorption band slightly moves to a shorter wavelength as the temperature rises. The temperature sensitivity of absorbance spectrum of water has been

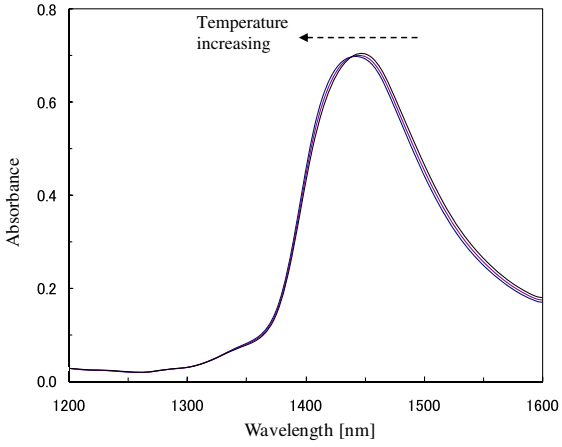

Fig. 1. Absorbance spectra of 0.5-mm thick water at 24.0 °C, 32.0 °C, and 40.0 °C.

known in NIR spectrometry [24–28]. We thus used T as an independent variable for A and I in Eq. (1). This temperature dependence is explained in terms of hydrogen bonds (H-bonds) between water molecules [24,36]. H-bonds lower the frequency of their intramolecular vibration; i.e., the existence of H-bonds shifts the original absorption bands to longer wavelengths. As the temperature increases, briefly, H-bonds become weaker and the number of H-bonds decreases. Consequently, the absorption bands shifts to shorter wavelengths as shown in Fig. 1.

To clarify the spectral change due to temperature, we defined an absorbance difference, $\Delta A(\lambda, T)$, by subtracting a reference absorbance spectrum, A_r, from an arbitrary one, A:

$$\Delta A = A - A_r = -\log_{10}\frac{I}{I_0} + \log_{10}\frac{I_r}{I_0}, \tag{2}$$

where λ and T are omitted for simplicity. I_r represents the intensity of transmitted light as a reference condition.

If I_0 is constant throughout measurements, ΔA can be calculated as follows:

$$\Delta A = -\log_{10}\frac{I}{I_r}. \tag{3}$$

Fig. 2 shows ΔA over the temperature range from 24.0 °C to 40.0 °C with a 2.0 K increment, where A at 24.0 °C has been chosen as A_r. A positive peak at 1412 nm and a negative one at 1488 nm can be seen. In this study, the wavelength of 1412 nm is used for the temperature imaging because its temperature sensitivity (peak amplitude) is the highest in the wavelength region. The wavelength of 1412 nm is represented by λ_T.

2.2. Apparatus

We used a general biological microscope (BX-51WI, Olympus, Japan) whose optical components had been replaced with NIR-transparent ones. The halogen lamp of the microscope emitted light from the visible to NIR. An NIR camera (Alpha NIR™, FLIR Systems, MA, USA) was mounted on the trinocular tube of the microscope. The detector of the camera was a 320 (H) × 256 (V) indium gallium arsenide (InGaAs) array covering a wavelength range from 900 nm to 1700 nm. An IR objective lens with 10-fold magnification was used. The observation area on the sample was 430 μm (H) × 345 μm (V). The 12-bit digital image data were recorded at 30 frames/s with image acquisition software (IRvista™, FLIR Systems, MA, USA). The gain and offset of each pixel, including fixed pattern noise, was compensated beforehand to be uniform by using calibration data provided with the software.

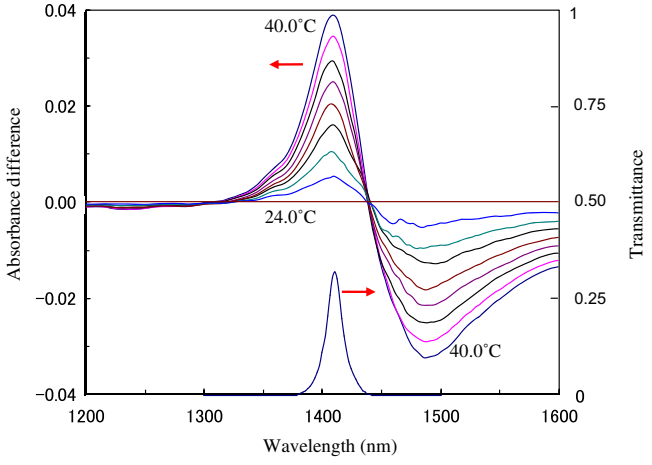

Fig. 2. Absorbance difference spectra (left scale) of 0.5-mm thick water over the temperature range from 24.0 °C to 40.0 °C in 2.0 K increments (the absorbance at 24.0 °C is the reference) and transmittance spectrum (right scale) of the narrow-bandpass filter.

To detect the light intensity at λ_T selectively, a narrow-bandpass filter was inserted between the light source and the sample in the microscope. The peak of the transmittance spectrum of the filter was at λ_T, and its bandwidth was quite narrow (Fig. 2). The filter also cut off the light of longer wavelengths and prevented unnecessary light absorption in a sample.

2.3. Absorbance for temperature imaging

When an optical filter with a transmittance spectrum of $\tau(\lambda)$ is put between a light source and a sample, the intensity of light transmitted through the sample, I, can be expressed as follows by using Eq. (1) and τ.

$$I(\lambda, T) = \tau(\lambda) I_0(\lambda) \times 10^{-A(\lambda,T)-\alpha(\lambda)}. \tag{4}$$

Integrating over the wavelength in the range from λ_1 to λ_2, we obtain the signal intensity for each pixel:

$$J = \int_{\lambda_1}^{\lambda_2} I\,\mathrm{d}\lambda + \varepsilon = \int_{\lambda_1}^{\lambda_2} \left\{\tau I_0 \times 10^{-A-\alpha}\right\}\mathrm{d}\lambda + \varepsilon, \tag{5}$$

where λ and T are omitted for simplicity. Symbol ε represents the noise intensity.

Because both I_0 and α are independent of wavelength from λ_1 to λ_2, the integrand in Eq. (5) can be changed as follows:

$$J = I_0'\alpha' \int_{\lambda_1}^{\lambda_2} \{\tau \times 10^{-A}\}\mathrm{d}\lambda + \varepsilon, \tag{6}$$

where

$$I_0' = I_0(\lambda) \quad \text{for} \quad \lambda_1 \le \lambda \le \lambda_2, \tag{7}$$

$$\alpha' = 10^{-\alpha(\lambda)} \quad \text{for} \quad \lambda_1 \le \lambda \le \lambda_2. \tag{8}$$

Now we define ΔB, the common logarithmic ratio of J to J_r (J for reference):

$$\Delta B \equiv -\log_{10}\frac{J}{J_r} = -\log_{10}\frac{\int_{\lambda_1}^{\lambda_2} I\,\mathrm{d}\lambda + \varepsilon}{\int_{\lambda_1}^{\lambda_2} I_r\,\mathrm{d}\lambda + \varepsilon_r}. \tag{9}$$

If I_0' is constant throughout measurements, Eq. (9) can be expressed as follows by using Eq. (6).

$$\Delta B = -\log_{10}\frac{\int_{\lambda_1}^{\lambda_2}\{\tau \times 10^{-A}\}\mathrm{d}\lambda + \varepsilon'}{\int_{\lambda_1}^{\lambda_2}\{\tau \times 10^{-A_r}\}\mathrm{d}\lambda + \varepsilon_r'} \tag{10}$$

where ε' is defined as:

$$\varepsilon' \equiv \frac{\varepsilon}{I_0'\alpha'}. \tag{11}$$

2.4. Samples

Pure water was put in a 0.5-mm thick flow-type quartz cuvette set on the microscope stage (Fig. 3). The sample temperature was controlled by putting a thermoplate (MATS-55RA20, Tokai Hit, Japan) on the microscope stage. The side and top faces of the cuvette, except for the area on the light path, were covered with metal blocks (not shown) for thermal uniformity. Furthermore, the sample was surrounded with an acrylic box on the stage to reduce environmental thermal effects. To form a temperature distribution through electric current heating, a nichrome wire with a length of 50 mm and diameter of 50 μm was inserted through the flow cuvette branches into the water. The wire was placed in the middle of the observation area (Fig. 4).

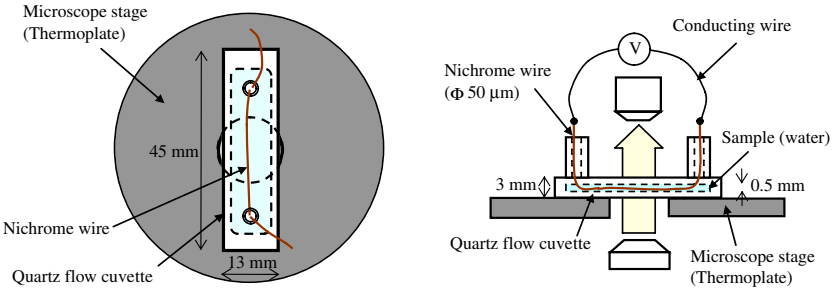

Fig. 3. Illustrations of a sample, as viewed from the top (left) and from the side (right).

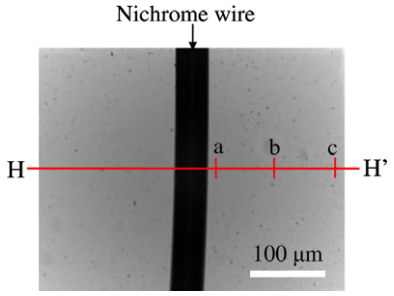

Fig. 4. Microscopic image of the water measurement region including a 50-μm diameter nichrome wire (center).

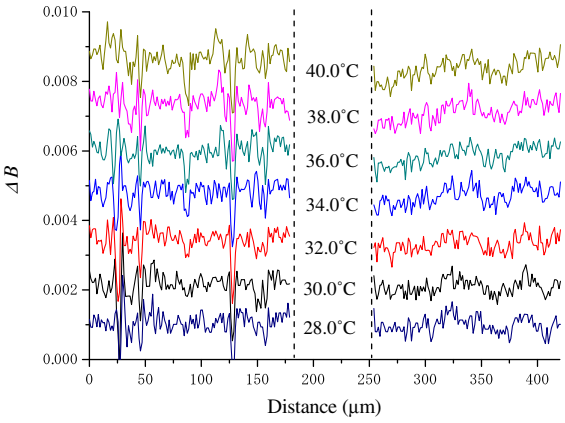

Fig. 5. Profiles of absorbance difference for imaging, ΔB, on the H–H′ line in Fig. 4 over the temperature range from 26.0 °C to 40.0 °C in 2.0 K increments (the absorbance at 26.0 °C is the reference).

2.5. Experimental protocols

To quantify the relationship between ΔB, as calculated by Eq. (9), and temperature, we acquired images from 26.0 °C to 40.0 °C in 2.0 K steps by raising the thermoplate's temperature. The water temperature was monitored by putting a 0.1-mm diameter thermocouple in the water. One hundred frames were acquired for each temperature. The pixel intensity of an average image of 100 frames at 26.0 °C was used as J_r to calculate ΔB for each temperature.

Next, without thermoplate heating, the water was intermittently heated (1-s heating and 2-s off cycle) with the hot nichrome wire giving 15.6 mW/(mm-wire) (3.0 V and 0.26 A). The reference intensity, J_r, was taken to be the intensity of each pixel of an image averaged over 100 frames before heating, and ΔB was calculated for all frames during heating. The Matlab image processing toolbox (Mathworks, MA, USA) was used for these calculations.

3. Measurement results

3.1. Calibration

Fig. 5 shows the profile of ΔB on the central horizontal line H–H′ (Fig. 4) in a frame for each temperature. The value of ΔB for each temperature was relatively uniform throughout the region, although there were differences in ΔB between pixels. A few dips in ΔB (e.g., at 127 μm) were due to small pieces of dirt in the water or on the glass. Since the histogram of ΔB of all pixels was similar to a normal distribution, we calculated the spatial average and standard deviation of ΔB for each temperature. The average ΔB plotted in Fig. 6 shows good linearity against temperature and its regression coefficient is $6.3 \times 10^{-4}\,\mathrm{K}^{-1}$. Actually, the linearity was expected because of the known linear relationship between $A(\lambda_T)$ and temperature [23,25]. Here, let us call the regression coefficient the 'temperature coefficient' and represent it by a_B. Eq. (9) can be accordingly rewritten as

$$a_B \Delta T = -\log_{10}\frac{J}{J_r}. \tag{12}$$

The magnitude of J was obtained on a 12-bit scale. When $J_r = 3500$, as set in the experiments, Eq. (12) indicates that a one bit change in J is equivalent to 0.2 °C.

The standard deviation of ΔB was approximately 5.2×10^{-4} for every temperature (minimum: 4.6×10^{-4} at 32 °C; maximum: 5.3×10^{-4} at 38 °C). By using this value and Eq. (9) or original data of J, the standard deviation of J was calculated as 1.8, when $J_r = 3500$. The deviations can be mostly attributed to random noise because the signals of adjacent pixels were not correlated. The

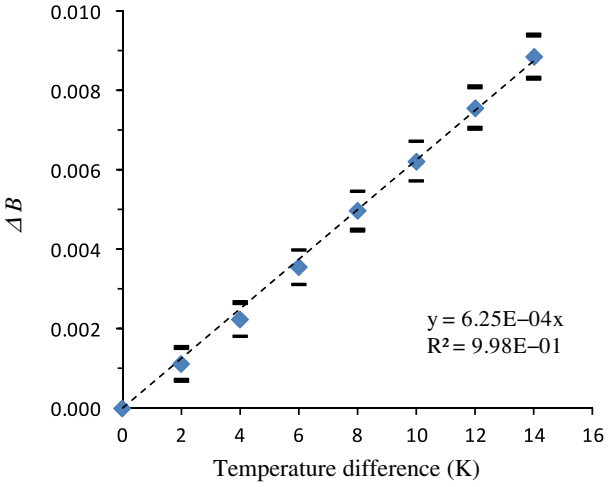

Fig. 6. Relationship between absorbance difference for imaging, ΔB, and temperature from 26.0 °C to 40.0 °C (the absorbance at 26.0 °C is the reference). Average (diamond) and standard deviation (bars) were calculated over all pixels of 100 frames for each temperature. R represents the correlation coefficient.

random noise must consist of optical shot noise and electrical noise. If the intensity of incident light had detectably fluctuated, it would have influenced the data of all pixels. Moreover, it is conceivable that changes in temperature in water were reflected in the random noises for the following reason: a change in temperature occurs only in a micro-region (1.3 μm × 1.3 μm) covered by one pixel would affect its surrounding temperatures through thermal diffusion during the frame interval (ca. 0.032 s), i.e., consider the problem of spatial pulse response. A simple parameter featuring the thermal diffusion can be calculated: 1.4×10^{-7} m^2/s × 0.032 s = 4.48×10^3 (μm)^2, where 1.4×10^{-7} m^2/s is the thermal diffusivity of water at 25 °C. This value is far greater than the coverage of a pixel, which points to the impossibility of detecting the temperature without correlation between pixels. This consideration also indicates that the standard deviation of J corresponds to the noise intensity, ε in Eq. (6) for each pixel.

An effective method for reducing such noise is spatial smoothing. Indeed, 3 × 3 pixel smoothing reduced the standard deviation to 1.9×10^{-4}, which is equivalent to 0.3 K according to a_B. If we consider thermal diffusion throughout an area corresponding to pixel, 3 × 3 pixel smoothing itself would not extinguish information about the temperature distribution. Accordingly, we applied 3 × 3 pixel smoothing to all frames.

3.2. Wire heating

Fig. 7 shows a series of ΔB images in the first heating period (<1 s), where the time of 0 s is defined as the start time of heating. Temporal changes in the temperature distribution due to thermal conduction from the hot wire were visualized. The temperature was almost uniform in the wire direction. Fig. 8 shows a series of ΔB profiles on the H–H′ line. The temperature rose in the vicinity of the wire at 0.03 s, whereas no rise occurred farther from it, even at 0.10 s. The rate of the rise gradually decreased near the wire. Here, a ΔB of 0.001 corresponds to a temperature difference of 1.6 K, based on the calibration results. Fig. 9 shows the evolution of ΔB at three different pixels marked a, b, and c in Fig. 4. Each profile faithfully reflects the heating cycle and the distance from the wire. Also note that the signals did not completely return to their initial levels within the cooling period. These results seem reasonable based on the knowledge of heat transfer, but they still need to be validated.

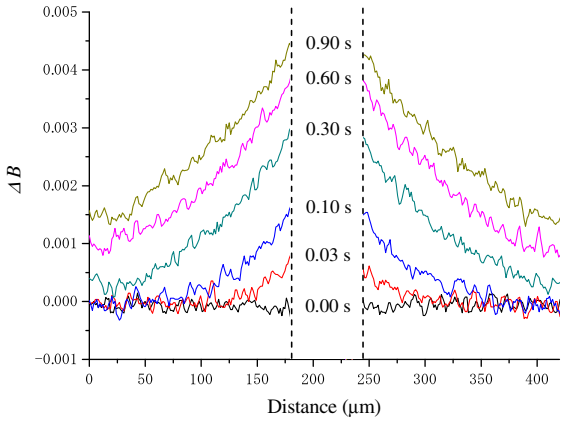

Fig. 8. Temporal change in absorbance difference, ΔB, on the H–H′ line in Fig. 4 after water was heated by the nichrome wire.

4. Validation

4.1. Calculation model

The calculation was done on a two-dimensional geometrical model consisting of a water layer, two quartz glass layers, and a heating element, similarly to the experimental sample (Fig. 10). Considering the symmetry of the geometrical model, the calculation used only one-quarter of the whole region (1.25 mm × 1.25 mm). It was assumed that thermal convection in water can be neglected and thermal conduction dominated heat transfer in the water and glass layers. A finite volume method was employed

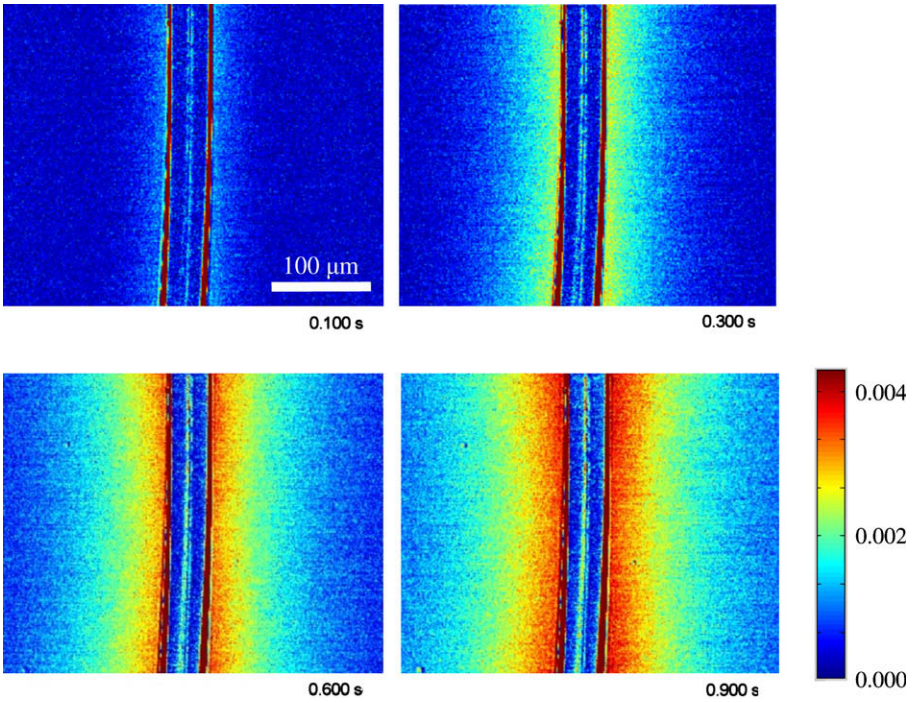

Fig. 7. Images of absorbance difference, ΔB, at 0.10 s (top left), 0.30 s (top right), 0.60 s (bottom left), and 0.90 s (bottom right) after water was heated by a nichrome wire.

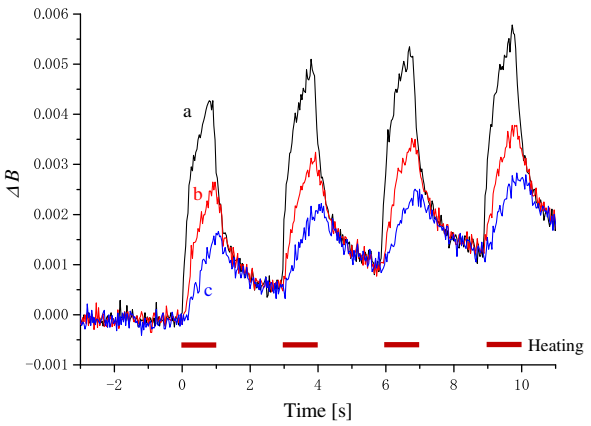

Fig. 9. Temporal change in absorbance difference, ΔB, at pixel (a) (15 μm from the right side of the wire), (b) (85 μm), and (c) (155 μm) on the H–H′ line in Fig. 4 during intermittent heating with the wire.

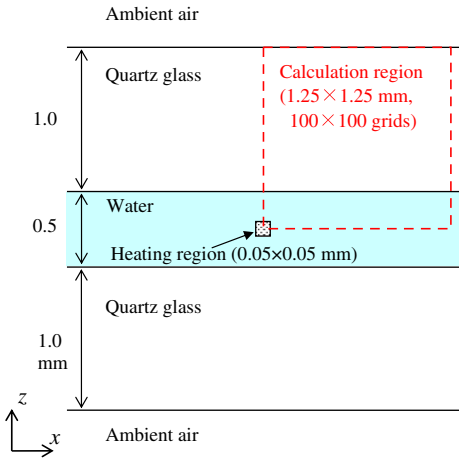

Fig. 10. Geometrical model for thermal conduction calculation. The model consists of a water layer, glass layers, and a heating region. Due to symmetry, the calculation only had to be done in a one-quarter region.

to discretize the unsteady-state thermal conduction equation as follows:

$$\rho c\frac{\partial T}{\partial t} = \nabla \cdot k\nabla T + M \tag{13}$$

where t is time, k thermal conductivity, ρ mass density, c specific heat capacity, and M the heat production rate. The thermal properties of each material are tabulated in Table 1. The value of M of the heating element was that of the hot wire in the experiment. The initial temperatures were 26.0 °C for all regions.

A convective heat transfer condition was used for the boundary between the glass surface and ambient air.

$$\frac{\partial T}{\partial z} = -\frac{h_a}{k}(T - T_a), \tag{14}$$

Table 1
Thermal properties used in the calculation.

Property	Water	Glass	Heating element
k (W/(m K))	0.56	1.40	17.40
ρ (kg/m^3)	993.3	2650.0	8670.0
c (J/(kg K))	4182.0	840.0	444.0
M (W/m^3)	0	0	6.55×10^9

where h_a is the convective heat transfer coefficient and T_a is the air temperature. We assumed that $h_a = 12.0$ W/(m^2 K) in the natural convection range. Symmetric conditions were used for the rest of the outer boundaries.

4.2. Results

Fig. 11 shows the calculated temperature distributions on the x–z plane in the part of the one-quarter water region (600 μm × 250 μm) at 0.1 s, 0.2 s, and 1.0 s after the start of heating. At 0.10 s, temperature rises in the vicinity of the heating region, but not at a distance of >150 μm from the center of the heating region. At 1.0 s, the temperature rise of >1 K is apparent even at 215 μm, a size over the image frame in experiment. In the glass layer, no significant rise in temperature was observed at 1.0 s (result not shown). For the sake of comparison with the temperature images of the experiments, the calculated temperatures were averaged along the z-direction throughout the x-coordinate.

Fig. 12 shows measured and calculated temperatures on the H–H′ line (right half), whereby the ΔB values were changed into temperatures by using the temperature coefficient. Although there are somewhat differences between the measured and calculated temperature profiles (maximum is approximately 1 K), they are a good match.

5. Discussion

The time-lapse series of temperature images demonstrated the process of thermal diffusion from a heating wire in water. The measured temperature distributions matched the calculated ones. The main reason for this can be that in a short period (<1.0 s) and microscale the contribution of thermal conduction to the temperature distributions was remarkably larger than those of other heat transfer modes such as natural convection in water. The simplicity of geometry and the reliability of thermal properties could contribute to the agreement. We also confirmed that the variation of h_a in a natural convection range did not affect the results. One of the factors leading to the discrepancy may be that in experiments the heating wire was not located in the center of the water layer. If the heating wire lies near the glass surface, measured temperatures will be lower than calculated ones. At any rate, these comparisons assured us that the images obtained by our imaging system faithfully reflected the temperature distributions of water.

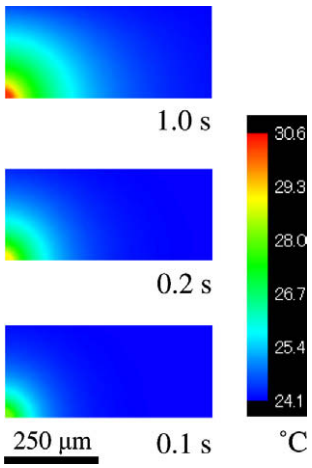

Fig. 11. Temporal change in calculated temperature distribution in the water region (one-quarter).

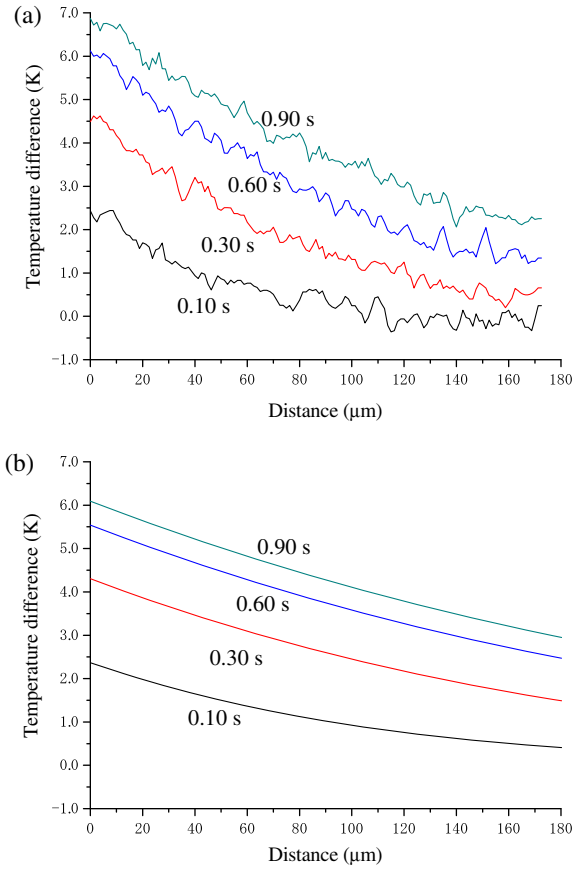

Fig. 12. (a) Measurement temperatures and (b) calculated temperatures at 0.10 s, 0.30 s, 0.60 s, and 0.90 s on the right half of the H−H′ line in Fig. 4. The horizontal scale indicates the distance from the heating element.

The temperature coefficient, a_B, is a factor determining the temperature resolution. If another bandpass filter narrower than the present one (we suppose narrow enough) is used in our apparatus, the value of a_B will improve. However, it is impossible for a_B to exceed the temperature coefficient for $A(\lambda_T)$, represented by a_A (=2.38 × 10^{-3} K^{-1}), which is the theoretical limit for an NIRS-based method using the $\nu_1 + \nu_3$ band. Meanwhile, a_B and a_A are proportional to a sample thickness as well as A. Fig. 13 shows the values of a_B for thicknesses from 0.05 to 1.5 mm, predicted from that for 0.5 mm. For comparison, the figure also shows the values of a_A. The increase in a_B with thickness indicates that a thicker sample would have better temperature resolution. However, the intensity

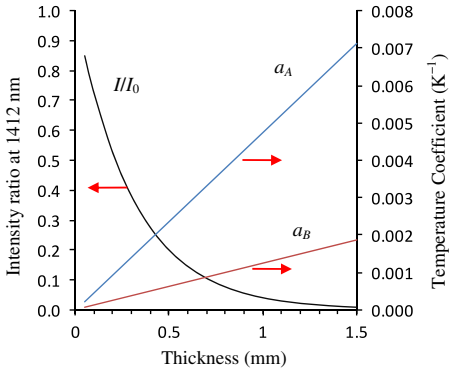

Fig. 13. Dependences of temperature coefficients, a_A and a_B (right scale), and intensity ratio, I/I_0, at 1412 nm (left scale) on the thickness of water.

of detected light, J, will become weaker if a thicker sample were used. Thus, both a_B and J determine the thickness range available for imaging and the temperature resolution.

Fig. 13 superposes the intensity ratio, I/I_0, at λ_T. By definition, I/I_0 is inversely proportional to the exponential of thickness, indicating that very little signal of I can be detected through a fairly thick sample. Strengthening the intensity of incident light, I_0, could solve this problem to some degree. However, there would be practical constraints on the light source itself and from the temperature of the sample rising too high due to excessive absorption. Therefore, although an effective range of thickness cannot be strictly determined, the relationship between a_B and I/I_0 and previous studies on NIRS suggest that a sub-millimeter-thickness could be a rough target sample range.

The use of absorption bands other than the $\nu_1 + \nu_3$ band could be a way to expand the usable range of thickness. The absorption band near 1910 nm, corresponding to the combination of the O–H bending mode and antisymmetric O–H stretching mode, ν_2 (ca. 1595 cm^{-1}) + ν_3 (ca. 3756 cm^{-1}), would be useful for a thinner sample because its absorbance and temperature coefficient are larger than those of the $\nu_1 + \nu_3$ band [24,26]. Indeed, by analyzing spectra of the $\nu_2 + \nu_3$ band, we predicted the temperatures of water less than 0.1 mm thick [22]. Note, however, that InGaAs detectors cannot cover the $\nu_2 + \nu_3$ band.

The effect of solutes on the temperature images must be investigated. Various solutes such as ions, alcohol, and saccharide certainly affect the H-bonds and vibrations of water molecules [38]. Given a practical concentration of each solute, however, the absorption bands of water would be still dominant and their spectra would not be deformed much. Otal et al. [29] measured the temperatures of four dilute aqueous solutions (NaCl, $NaHCO_3$, NaOH, and HCl 0.1 M solutions) using NIRS and found no significant effect on temperature predictions, despite slight changes in absorbance (an accuracy of 0.5 K was assured from 15 to 90 °C). A lot of studies indicate that although the absorption band of glucose partly overlaps the $\nu_1 + \nu_3$ band of water, the change in absorbance due to temperature is larger than the change due to glucose in a practical concentration range. Hence, glucose is difficult to measure with a non-invasive method.

An observable solute effect on the absorption spectrum of water would be mostly due to a decrease in water content rather than hydration of solute [23]. This is analogous to the change in thickness; i.e., as the water content decreases, the absorbance and temperature coefficient will proportionally decrease. It would be difficult to predict the effect of this factor on an arbitrary sample. However, it is almost inconceivable that the concentration of a solute dramatically increases or decreases enough to change the water content considerably during a measurement. Accordingly, if the absorption band of water can be initially recognized, temperature imaging can be applied. For turbid (scattering) solutions, on the other hand, it may be difficult to obtain correct temperature distributions because the pathway and path length of light traveling through the sample vary spatially and temporally [23,39]. A compensation method will be needed in devices and image processing, which is a subject for a future study.

6. Conclusion

A temperature imaging method based on the temperature dependence of the NIR absorption of water has been presented. The apparatus consists of a microscope, NIR camera, and narrow-bandpass filter for measuring the absorbance at 1412 nm. The method is convenient because neither excitation light nor marker particle mixed in a sample is needed for measurement. Calibration results for 0.5-mm thick water from 26.0 °C to 40.0 °C demonstrated a linear relationship between absorbance and temperature.

The temperature coefficient was $6.3 \times 10^{-4}\,K^{-1}$, and the standard deviation of absorbance was 1.9×10^{-4}. After that, thermal diffusion in 0.5-mm thick water with a thin heating wire in it was visualized. The obtained images were verified with temperatures calculated with a two-dimensional model for thermal conduction. The present imaging method would have chemical, biomedical, and industrial applications for measuring the temperature distributions of aqueous solutions, aqueous gels, and biological samples with thermogenic reactions in μ-TAS or biochip analyses. These applications should be addressed in a future work.

Acknowledgment

This work was supported in part by a Grand-in-Aid for Young Scientists (A) No. 18686019 of the Ministry of Education, Culture, Sports, Science and Technology of Japan.

References

[1] P.S. Dittrich, K. Tachikawa, A. Manz, Micro total analysis systems: latest advancements and trends, Anal. Chem. 78 (12) (2006) 3887–3908.
[2] B. Xie, K. Ramanathan, B. Danielsson, Mini/micro thermal biosensors and other related devices for biochemical/clinical analysis and monitoring, Trends Anal. Chem. 19 (5) (2000) 340–349.
[3] V. Krivtzun, B. Graß, R. Hergenroder, M. Bolshov, K. Niemax, A. Zybin, Temperature measurement of liquids by differential absorption of two diode lasers: application of contactless optical detection in isotachophoresis, Appl. Spectrosc. 55 (9) (2001) 1251–1258.
[4] T. Schwalbe, V. Autze, G. Wille, Chemical synthesis in microreactors, Chimia 56 (2002) 636–646.
[5] E.A. Johannessen, J.M.R. Weaver, L. Bourova, P. Svoboda, P.H. Cobbold, J.M. Cooper, Micromachined nanocalorimetric sensor for ultra-low-volume cell-based assays, Anal. Chem. 74 (9) (2002) 2190–2197.
[6] J.-L. Garden, E. Chateau, J. Chaussy, Highly sensitive ac nanocalorimeter for microliter-scale liquids or biological samples, Appl. Phys. Lett. 84 (18) (2004) 3597–3599.
[7] Y. Zhang, S. Tadigadapa, Calorimetric biosensors with integrated microfluidic channels, Biosens. Bioelectron. 19 (2004) 1733–1743.
[8] Q. Zhang, W. Wang, H. Zhang, Y. Wang, Temperature analysis of continuous-flow micro-PCR based on FEA, Sensor Actuator 82 (2002) 75–81.
[9] S.H. Kim, J. Noh, M.K. Jeon, K.W. Kim, L.P. Lee, S.I. Woo, Micro-Raman thermometry for measuring the temperature distribution inside the microchannel of a polymerase chain reaction chip, J. Micromech. Microeng. 16 (2006) 526–530.
[10] T.-M. Hsieh, C.-H. Luo, F.-C. Huang, J.-H. Wang, L.-J. Chien, G.-B. Lee, Enhancement of thermal uniformity for a microthermal cycler and its application for polymerase chain reaction, Sensor Actuator B 130 (2008) 848–856.
[11] O. Fudym, C. Pradère, J.-C. Batsale, An analytical two-temperature model for convection–diffusion in multilayered systems: application to the thermal characterization of microchannel reactors, Chem. Eng. Sci. 62 (2007) 4054–4064.
[12] N. Sahba, T.J. Rockett, Infrared absorption coefficients of silica glasses, J. Am. Ceram. Soc. 75 (1) (1992) 209–212.
[13] A.S. Merschman, S.H. Lubbad, D.C. Tilotta, Poly(dimethylsiloxane) films as sorbents for solid-phase microextraction coupled with infrared spectroscopy, J. Chromatogr. A 829 (1998) 377–384.
[14] P.R.N. Childs, J.R. Greenwood, C.A. Long, Review of temperature measurement, Rev. Sci. Instrum. 71 (8) (2000) 2959–2978.
[15] H.J. Kim, K.D. Kihm, J.S. Allen, Examination of ratiometric laser induced fluorescence thermometry for microscale spatial measurement resolution, Int. J. Heat Mass Transfer 46 (2003) 3967–3974.
[16] C.F. Chapman, Y. Liu, G.J. Sonek, B.J. Tromberg, The use of exogenous fluorescent probes for temperature measurements in single living cells, Photochem. Photobiol. 62 (3) (1995) 416–425.
[17] M.N. Slyadnev, Y. Tanaka, M. Tokeshi, T. Kitamori, Photothermal temperature control of a chemical reaction on a microchip using an infrared diode laser, Anal. Chem. 73 (16) (2001) 4037–4044.
[18] A.V. Kachynski, A.N. Kuzmin, H.E. Pudavar, P.N. Prasad, Three-dimensional confocal thermal imaging using anti-Stokes luminescence, Appl. Phys. Lett. 87 (2005) 023901.
[19] C. Gota, S. Uchiyama, T. Ohwada, Accurate fluorescent polymeric thermometers containing an ionic component, Analyst 132 (2007) 121–126.
[20] R. Muwanga, I. Hassan, Local heat transfer measurements in microchannels using liquid crystal thermography: methodology development and validation, ASME J. Heat Trans. 128 (2006) 617–626.
[21] N. Kakuta, A. Ozaki, F. Li, H. Arimoto, Y. Yamada, Measurement of temperature differences between micro-regions in water using near-infrared spectroscopy, Proc. 29th Ann. Intl. Conf. IEEE EMBS (2007) 4564–4567.
[22] N. Kakuta, A. Ozaki, H. Arimoto, Y. Yamada, Temperature measurements of micro-regions in water using near-infrared spectroscopy, Proc. 8th Asian Thermophys. Prop. Conf. (2007) 023 (1–6).
[23] N. Kakuta, H. Arimoto, H. Momoki, F. Li, Y. Yamada, Temperature measurements of turbid aqueous solutions using near-infrared spectroscopy, Appl. Opt. 47 (13) (2008) 2227–2233.
[24] D. Eisenberg, W. Kauzmann, The Structure and Properties of Water, Oxford at the Clarendon Press, London, 1969.
[25] J. Lin, C.W. Brown, Near-IR fiber-optic temperature sensor, Appl. Spectrosc. 47 (1) (1993) 62–68.
[26] F.O. Libnau, O.M. Kvalheim, A.A. Christy, J. Toft, Spectra of water in the near- and mid-infrared region, Vib. Spectrosc. 7 (1994) 243–254.
[27] V.H. Segtnan, S. Sasic, T. Isaksson, Y. Ozaki, Studies on the structure of water using two-dimensional near-infrared correlation spectroscopy and principal component analysis, Anal. Chem. 73 (13) (2001) 3153–3161.
[28] V.S. Hollis, T. Binzoni, D.T. Delpy, Non-invasive monitoring of brain tissue temperature by near-infrared spectroscopy, Proc. SPIE 4250 (2001) 470–481.
[29] E.H. Otal, F.A. Inon, F.J. Andrade, Monitoring the temperature of dilute aqueous solutions using near-infrared water absorption, Appl. Spectrosc. 57 (6) (2003) 661–666.
[30] S.A. Thompson, F.J. Andrade, F.A. Inon, Light emission diode water temperature: a low-cost and noninvasive strategy for monitoring temperature in aqueous solutions, Appl. Spectrosc. 58 (3) (2004) 344–348.
[31] H. Arimoto, M. Tarumi, Y. Yamada, Temperature-insensitive measurement of glucose concentration based on near infrared spectroscopy and partial least squares analysis, Opt. Rev. 10 (2) (2003) 74–76.
[32] P.S. Jensen, J. Bak, S. Andersson-Engels, Influence of temperature on water and aqueous glucose absorption spectra in the near- and mid-infrared regions at physiologically relevant temperatures, Appl. Spectrosc. 57 (1) (2003) 28–36.
[33] S.-j. Yeh, C.F. Hanna, O.S. Khalil, Monitoring blood glucose changes in cutaneous tissue by temperature-modulated localized reflectance measurements, Clin. Chem. 49 (6) (2003) 924–934.
[34] H. Cui, L. An, W. Chen, K. Xu, Quantitative effect of temperature to the absorbance of aqueous glucose in wavelength range from 1200 nm to 1700 nm, Opt. Express 13 (2005) 6887–6891.
[35] M.A. Khashan, A.Y. Nassif, Dispersion of the optical constants of quartz and polymethyl methacrylate glasses in a wide spectral range: 0.2–3 μm, Opt. Commun. 188 (2001) 129–139.
[36] L. Bokobza, Origin of near-infrared absorption bands, in: H.W. Siesler, Y. Ozaki, S. Kawata, H.M. Heise (Eds.), Near-Infrared Spectroscopy, Wiley-VCH, Weinheim, Germany, 2002, pp. 11–41.
[37] H.W. Siesler, Applications to polymers and textiles, in: H.W. Siesler, Y. Ozaki, S. Kawata, H.M. Heise (Eds.), Near-Infrared Spectroscopy, Wiley-VCH, Weinheim, Germany, 2002, pp. 213–245.
[38] K. Masuda, T. Haramaki, S. Nakashima, B. Habert, I. Martinez, S. Kashiwabara, Structural change of water with solutes and temperature up to 100 °C in aqueous solutions as revealed by attenuated total reflectance infrared spectroscopy, Appl. Spectrosc. 57 (3) (2003) 274–281.
[39] V.A. McGlone, P. Martinsen, R. Kunnemeyer, B. Jordan, B. Cletus, Measuring optical temperature coefficients of intralipid, Phys. Med. Biol. 52 (2007) 2367–2378.